



# Stability analysis of internally damped rotating composite shafts using a finite element formulation



Safa Ben Arab<sup>a,b,\*</sup>, José Dias Rodrigues<sup>a</sup>, Slim Bouaziz<sup>b</sup>, Mohamed Haddar<sup>b</sup>

<sup>a</sup> Faculty of Engineering, University of Porto, Portugal

<sup>b</sup> Laboratory of Mechanics, Modeling and Production, LA2MP, National Engineering School of Sfax, University of Sfax, Tunisia

## ARTICLE INFO

### Article history:

Received 1 June 2017

Accepted 8 January 2018

Available online 12 January 2018

### Keywords:

Rotating shaft

Composite material

Internal damping

Finite element method

Stability analysis

## ABSTRACT

This paper deals with the stability analysis of internally damped rotating composite shafts. An Euler–Bernoulli shaft finite element formulation based on Equivalent Single Layer Theory (ESLT), including the hysteretic internal damping of composite material and transverse shear effects, is introduced and then used to evaluate the influence of various parameters: stacking sequences, fiber orientations and bearing properties on natural frequencies, critical speeds, and instability thresholds. The obtained results are compared with those available in the literature using different theories. The agreement in the obtained results show that the developed Euler–Bernoulli finite element based on ESLT including hysteretic internal damping and shear transverse effects can be effectively used for the stability analysis of internally damped rotating composite shafts. Furthermore, the results revealed that rotor stability is sensitive to the laminate parameters and to the properties of the bearings.

© 2018 Académie des sciences. Published by Elsevier Masson SAS. All rights reserved.

## 1. Introduction

A precise prediction of damping effects is basically necessary in the stability analysis of rotor dynamic behaviour. Damping is considered as an internal damping such as material damping or as an external damping as in the case of bearing damping, and it is principally modeled using viscous or hysteretic damping. The basic difference between viscous and hysteretic models is that the dissipation of energy by viscous damping depends on frequency, while the dissipation of energy by hysteretic damping does not. In composite rotor dynamic field, internal damping can be meaningful because of the damping capacity of the matrix [1]. Moreover, most materials, such as metallic materials, carbon/epoxy materials, and viscoelastic materials show a vibratory damping behaviour that looks like hysteretic internal damping much more than like viscous internal damping [2]. Due to the specific strength and stiffness of the fiber-reinforced composite materials, metal shafts have been replaced by composite shafts in many applications, such as drive shafts for helicopters and automotive industries [3–7]. These materials offer benefits in terms of reduction of the weight and augmentation of the strength, stiffness and damping capacity, and provide structural designers the possibility of obtaining required behaviours by changing the stacking sequence of the composite layers in terms of number and orientation of layers [8,9].

Many researchers studied the damping effects on rotor dynamic and stability behaviour [1,2,10–15]. First investigations by Newkirk [10] showed that rotors may undergo violent whirling at speeds above the first critical speed because of in-

\* Corresponding author at: Laboratory of Mechanics, Modeling and Production, LA2MP, National Engineering School of Sfax, University of Sfax, Tunisia.  
E-mail address: safabenarab@gmail.com (S. Ben Arab).

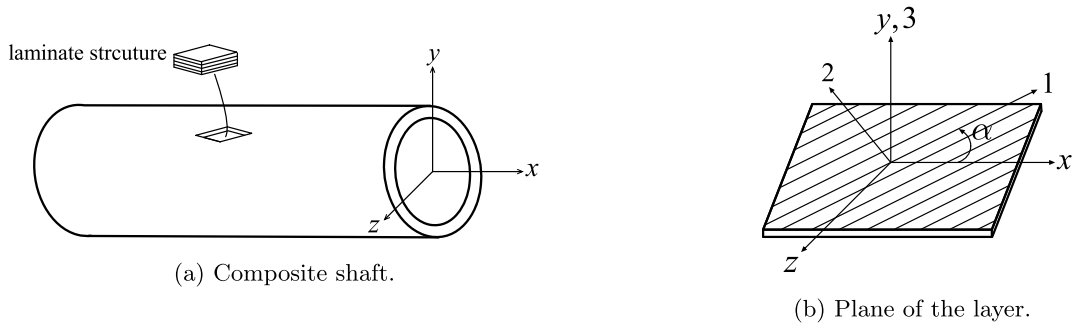


Fig. 1. Composite shaft.

ternal damping. After that, Genta [12] explained similarly that the hysteretic internal damping of the rotating elements of a structure is stabilizing in the subcritical range and destabilizing in the supercritical range; they proved that an error is made when admitting that hysteretic internal damping of rotating elements is destabilizing at all rotational speeds. Montagnier and Hochard [2] demonstrated likewise that damping associated with the non-rotating elements of the structure has a stabilizing effect, while damping associated with the rotating elements may provoke instability in the supercritical range. Besides, many researchers have studied the combined influence of internal and external damping. The results show that rotor stability is enhanced by increasing bearing damping; however, increasing internal damping can reduce the instability threshold [11,16]. Pereira and Silveira [11] used an optimization techniques to avoid the instability, reduce the unbalanced response, and augment the stability limit speed. They adopted the Equivalent Modulus Beam Theory (EMBT) developed by Singh and Gupta [17,18]. In fact, EMBT has many limitations and is only valid for symmetric stacking sequences. Simplified Homogenized Beam Theory (SHBT) based on Timoshenko’s beam theory has been developed by Sino et al. [14] to consider the effects of the stacking sequence and internal damping of composite material. Jacquet-Richardet et al. [15] illustrated and validated the theoretical formulation proposed by Sino et al. [14] by developing an experimental setup to analyse the dynamic instability of an internally damped rotating composite shaft. More recently, Ben Arab et al. [19] developed ESLT based on Timoshenko’s beam theory to consider the effects of stacking sequence, fiber orientations, and shear-normal coupling. ESLT considers the laminated shaft made of several orthotropic layers as an equivalent single layer having mechanical properties equivalent to those of all the layers. The authors proved that ESLT is quite adequate for the dynamic analysis of rotating composite shafts in both symmetric and non-symmetric stacking sequences.

In this paper, an Euler–Bernoulli shaft finite element formulation based on Equivalent Single Layer Theory (ESLT) is adopted. ESLT consists in considering a laminated shaft made of several orthotropic layers as an equivalent single layer having mechanical properties equivalent to those of all the layers [19,20]. The developed formulation considers the translatory, rotary inertia, and gyroscopic effects as well as the shear transverse effect that was introduced in the shape functions. This formulation is developed to analyse the effects of hysteric internal damping, fiber orientation, and stacking sequence on natural frequencies, critical speeds, and instability thresholds of internally damped rotating composite shafts. The technical contribution of the present investigation is to study the stability behaviour of internally damped rotating composite shaft considering the shear transverse effect by developing an Euler–Bernoulli shaft finite element formulation based on Equivalent Single Layer Theory (ESLT). A brief description of the theoretical background concerning the hysteretic internal damping modeling is presented. First, the kinetic energy  $T$  and the deformation energy  $\Pi$  of the rotor system are established. Then, the finite element method is employed, and the equation of motion is determined using Lagrange’s equations.

## 2. Composite shaft

The composite shaft is obtained by winding several layers of embedded fibers on a mandrel. Each layer has an orthotropic mechanical behaviour (see Fig. 1).

The generalized Hooke law for an orthotropic material is given by:

$$\{\sigma\} = [Q]\{\varepsilon\} \tag{1}$$

where  $\{\sigma\}$  and  $\{\varepsilon\}$  are, respectively, the stress and the strain fields, and  $[Q]$  is the material stiffness matrix. When linked to the orthotropic axis, each layer can be characterized by a plane stress state. So, one gets:

$$\begin{Bmatrix} \sigma_1 \\ \sigma_2 \\ \tau_{23} \\ \tau_{31} \\ \tau_{12} \end{Bmatrix} = \begin{bmatrix} \frac{E_1}{1-\nu_{12}\nu_{21}} & \frac{\nu_{12}E_2}{1-\nu_{12}\nu_{21}} & 0 & 0 & 0 \\ \frac{\nu_{12}E_2}{1-\nu_{12}\nu_{21}} & \frac{E_2}{1-\nu_{12}\nu_{21}} & 0 & 0 & 0 \\ 0 & 0 & G_{23} & 0 & 0 \\ 0 & 0 & 0 & G_{13} & 0 \\ 0 & 0 & 0 & 0 & G_{12} \end{bmatrix} \begin{Bmatrix} \varepsilon_1 \\ \varepsilon_2 \\ \gamma_{23} \\ \gamma_{31} \\ \gamma_{12} \end{Bmatrix} \tag{2}$$

where the Young moduli  $E_1$  and  $E_2$ , the shear moduli  $G_{23}$ ,  $G_{13}$ , and  $G_{12}$ , and the Poisson ratios  $\nu_{12}$  and  $\nu_{21}$  are identified for each layer in the orthotropic axes (1, 2, 3): 1 is the fiber orientation, 2 is the transversal direction to the fibers, and 3 is the perpendicular direction to the layer as shown in Fig. 1b.

The stress–strain relation for a composite shaft including the hysteretic internal damping is given by [11]:

$$\{\sigma\} = [Q]\{\varepsilon\} + [Q]^\psi \{\dot{\varepsilon}\} \tag{3}$$

where  $[Q]^\psi = [Q][\eta]$  is the damped material stiffness matrix and  $[\eta]$  is the damping matrix of the layer, which can be linked to the specific damping capacity matrix  $[\psi]$  as follows:

$$[\eta] = \frac{1}{2\pi} [\psi] \tag{4}$$

The dissipative properties of the layer can also be expressed by using the specific damping capacity matrix  $[\psi]$  defined as:

$$[\psi] = \begin{bmatrix} \psi_1 & 0 & 0 & 0 & 0 \\ 0 & \psi_2 & 0 & 0 & 0 \\ 0 & 0 & \psi_{23} & 0 & 0 \\ 0 & 0 & 0 & \psi_{13} & 0 \\ 0 & 0 & 0 & 0 & \psi_{12} \end{bmatrix} \tag{5}$$

Consequently, the damped material stiffness matrix  $[Q]^\psi$  is expressed as a function of the specific damping capacity matrix  $[\psi]$  as:

$$[Q]^\psi = \frac{1}{2\pi} [Q][\psi] \tag{6}$$

Let consider an arbitrary layer of the laminate whose fiber orientation makes an angle  $\alpha$  with respect to the  $x$  axis, as shown in Fig. 1b. The stress–strain relation can be written in the global frame ( $x, y, z$ ) as:

$$\{\sigma\} = [\bar{Q}]\{\varepsilon\} + [\bar{Q}]^\psi \{\dot{\varepsilon}\} \tag{7}$$

where  $[\bar{Q}]$  is the transformed material stiffness matrix and  $[\bar{Q}]^\psi$  is the transformed damped material stiffness matrix of the layer:

$$[\bar{Q}] = [T]^T [Q] [T] \quad \text{and} \quad [\bar{Q}]^\psi = [T]^T [Q]^\psi [T] \tag{8}$$

where the transformation matrix  $[T]$  is given by [21]:

$$[T] = \begin{bmatrix} \cos^2 \alpha & \sin^2 \alpha & 0 & 0 & \cos \alpha \sin \alpha \\ \sin^2 \alpha & \cos^2 \alpha & 0 & 0 & -\cos \alpha \sin \alpha \\ 0 & 0 & \cos \alpha & -\sin \alpha & 0 \\ 0 & 0 & \sin \alpha & \cos \alpha & 0 \\ -2 \cos \alpha \sin \alpha & 2 \cos \alpha \sin \alpha & 0 & 0 & \cos^2 \alpha - \sin^2 \alpha \end{bmatrix} \tag{9}$$

The stress–strain relation expressed in Equation (7) can be written as follows:

$$\{\sigma\} = \begin{cases} \sigma_{xx} = \bar{Q}_{11} \varepsilon_{xx} + \bar{Q}_{11}^\psi \dot{\varepsilon}_{xx} \\ \tau_{xz} = k_s \bar{Q}_{55} \gamma_{xz} + k_s \bar{Q}_{55}^\psi \dot{\gamma}_{xz} \\ \tau_{xy} = k_s \bar{Q}_{66} \gamma_{xy} + k_s \bar{Q}_{66}^\psi \dot{\gamma}_{xy} \end{cases} \tag{10}$$

where  $k_s$  is the shear correction factor and  $\bar{Q}_{ij}$  and  $\bar{Q}_{ij}^\psi$  are the constitutive terms that are related to the fiber orientation angle  $\alpha$  and to the elastic constants of the principal axes of each orthotropic layer, as follows:

$$\begin{cases} \bar{Q}_{11} = \cos^4(\alpha) Q_{11} + \sin^4(\alpha) Q_{22} + \cos^2(\alpha) \sin^2(\alpha) (2Q_{12} + 4Q_{66}) \\ \bar{Q}_{55} = \sin^2(\alpha) Q_{44} + \cos^2(\alpha) Q_{55} \\ \bar{Q}_{66} = \cos^2(\alpha) \sin^2(\alpha) (Q_{11} + Q_{22} - 2Q_{12}) + (\cos^2(\alpha) - \sin^2(\alpha))^2 Q_{66} \end{cases} \tag{11}$$

$$\begin{cases} \bar{Q}_{11}^\psi = \cos^4(\alpha) \psi_1 Q_{11} + \sin^4(\alpha) \psi_2 Q_{22} + \cos^2(\alpha) \sin^2(\alpha) (\psi_1 Q_{12} + \psi_2 Q_{12} + 4\psi_{12} Q_{66}) \\ \bar{Q}_{55}^\psi = \sin^2(\alpha) \psi_{23} Q_{44} + \cos^2(\alpha) \psi_{13} Q_{55} \\ \bar{Q}_{66}^\psi = \cos^2(\alpha) \sin^2(\alpha) (\psi_1 Q_{11} + \psi_2 Q_{22} - \psi_1 Q_{12} - \psi_2 Q_{12}) + (\cos^2(\alpha) - \sin^2(\alpha))^2 \psi_{12} Q_{66} \end{cases} \tag{12}$$

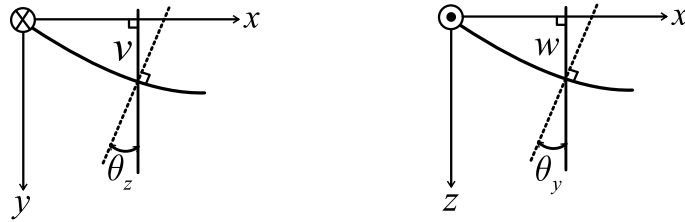


Fig. 2. Displacement field variables.

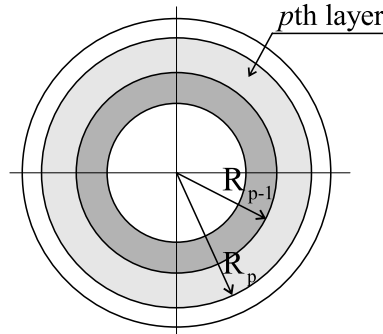


Fig. 3. Inner and outer radius of the pth layer of the composite shaft.

3. Kinetic and deformation energies

An Euler–Bernoulli shaft based on Equivalent Single Layer Theory (ESLT) is developed in this work. In fact, ESLT consists in considering a laminated shaft made of  $P$  orthotropic layers as an equivalent single orthotropic layer having mechanical properties equivalent to those of all the layers. Indeed, each orthotropic layer contributes with its fiber orientation and its distance from the shaft longitudinal axis [19].

The displacement field is described by transverse displacements  $v$  and  $w$  along the  $y$  and  $z$  directions, respectively, and the slopes  $\theta_y$  and  $\theta_z$  in  $x$ – $y$  and  $x$ – $z$  planes, respectively, as shown in Fig. 2.

3.1. Kinetic energy

Integrating over the shaft cross sectional area by summing up the contribution of each orthotropic layer, the kinetic energy of the rotating laminated shaft including the translatory, rotary inertia and gyroscopic effects is given by [19]:

$$T = \frac{1}{2} \int_0^L \left[ I_m (\dot{v}^2 + \dot{w}^2) + I_d (\dot{\theta}_y^2 + \dot{\theta}_z^2) - 2I_p \Omega \theta_y \dot{\theta}_z + I_p \Omega^2 \right] dx \tag{13}$$

where  $L$  is the length of the composite shaft. The mass quantity  $I_m$  denotes the mass per unit length of the composite shaft, while  $I_d$  and  $I_p$  denote respectively the diametrical and the polar moment of inertia of the shaft cross section, defined as:

$$\begin{cases} I_m = \pi \sum_{p=1}^P \rho_p (R_p^2 - R_{p-1}^2) \\ I_d = \frac{\pi}{4} \sum_{p=1}^P \rho_p (R_p^4 - R_{p-1}^4) \\ I_p = \frac{\pi}{2} \sum_{p=1}^P \rho_p (R_p^4 - R_{p-1}^4) \end{cases} \tag{14}$$

where  $P$  represents the number of layers,  $\rho_p$  is the mass density, and  $R_{p-1}$  and  $R_p$  are, respectively, the inner and the outer radius of the  $p$ th layer of the composite shaft as shown in Fig. 3. The term  $I_d (\dot{\theta}_y^2 + \dot{\theta}_z^2)$ , given in Equation (13), represents the rotary inertia effect and  $2I_p \Omega \theta_y \dot{\theta}_z$  accounts for the gyroscopic effect.

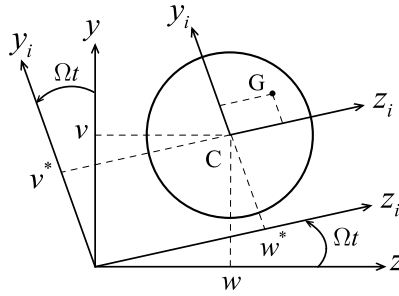


Fig. 4. Coordinates of the geometric center C and of an arbitrary point G in the shaft cross section axis system.

### 3.2. Deformation energy

Considering small deformations, the longitudinal strain subjected to the bending efforts is given by:

$$\epsilon_{xx} = z \frac{\partial \theta_y}{\partial x} - y \frac{\partial \theta_z}{\partial x} \tag{15}$$

Deriving the longitudinal strain expression (15) with respect to time, one gets:

$$\dot{\epsilon}_{xx} = z \frac{\partial \dot{\theta}_y}{\partial x} - y \frac{\partial \dot{\theta}_z}{\partial x} \tag{16}$$

According to the Euler–Bernoulli equations, the relations between the displacements  $v^*$  and  $w^*$  of the geometric center of the shaft cross section and the slopes  $\theta_y$  and  $\theta_z$  about the  $y$  and  $z$  axis, respectively, are given as:

$$\theta_y = -\frac{\partial w^*}{\partial x} \quad \text{and} \quad \theta_z = \frac{\partial v^*}{\partial x} \tag{17}$$

Substituting Equations (17) into Equations (15) and (16), one gets:

$$\begin{cases} \epsilon_{xx} = -z \frac{\partial^2 w^*}{\partial x^2} - y \frac{\partial^2 v^*}{\partial x^2} \\ \dot{\epsilon}_{xx} = -z \frac{\partial^2 \dot{w}^*}{\partial x^2} - y \frac{\partial^2 \dot{v}^*}{\partial x^2} \end{cases} \tag{18}$$

The composite shaft deformation energy is given by:

$$\Pi = \frac{1}{2} \int_V \epsilon^T \sigma \, dV \tag{19}$$

Considering the longitudinal strain subjected to the bending  $\epsilon_{xx}$  and using Equation (10), the internally damped composite shaft deformation energy can be expressed as:

$$\Pi = \frac{1}{2} \int_V \left( \bar{Q}_{11} \epsilon_{xx}^2 + \bar{Q}_{11}^\psi \epsilon_{xx} \dot{\epsilon}_{xx} \right) dV \tag{20}$$

Substituting Equations (18) into the composite shaft deformation energy expression (20) yields:

$$\Pi = \frac{1}{2} \int_V \bar{Q}_{11} \left( -z \frac{\partial^2 w^*}{\partial x^2} - y \frac{\partial^2 v^*}{\partial x^2} \right)^2 dV + \frac{1}{2} \int_V \bar{Q}_{11}^\psi \left( -z \frac{\partial^2 w^*}{\partial x^2} - y \frac{\partial^2 v^*}{\partial x^2} \right) \left( -z \frac{\partial^2 \dot{w}^*}{\partial x^2} - y \frac{\partial^2 \dot{v}^*}{\partial x^2} \right) dV \tag{21}$$

Accordingly to Fig. 4, the relations between the displacements  $v^*$  and  $w^*$  and the displacements  $v$  and  $w$  measured in the inertial axes system are:

$$\begin{cases} v^* = w \sin(\Omega t) + v \cos(\Omega t) \\ w^* = w \cos(\Omega t) - v \sin(\Omega t) \end{cases} \tag{22}$$

Deriving Equation (22) with respect to time, one gets the velocity expressions:

$$\begin{cases} \dot{v}^* = \dot{w} \sin(\Omega t) + w \Omega \cos(\Omega t) + \dot{v} \cos(\Omega t) - v \Omega \sin(\Omega t) \\ \dot{w}^* = \dot{w} \cos(\Omega t) - w \Omega \sin(\Omega t) - \dot{v} \sin(\Omega t) - v \Omega \cos(\Omega t) \end{cases} \tag{23}$$

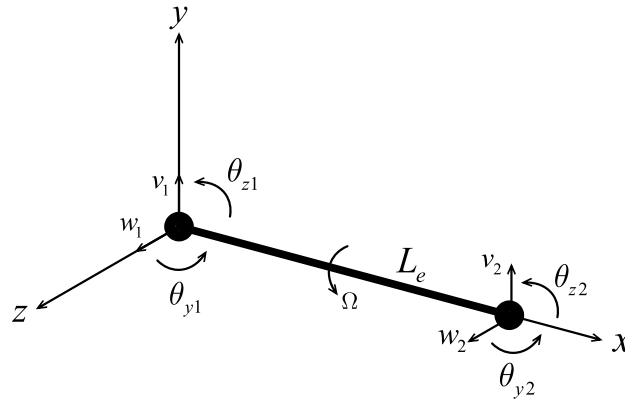


Fig. 5. Shaft finite element.

Substituting Equations (22) and (23) into composite shaft deformation energy expression (21) and integrating over the shaft cross sectional area by summing up the contribution of each orthotropic layer, the internally damped composite shaft deformation energy can be expressed as:

$$\begin{aligned}
 \Pi = & \frac{1}{2} A_{11} \int_0^L \left[ \left( \frac{\partial^2 v}{\partial x^2} \right)^2 + \left( \frac{\partial^2 w}{\partial x^2} \right)^2 \right] dx \\
 & + \frac{1}{2} A_{11}^\psi \int_0^L \left[ \left( \frac{\partial^2 v}{\partial x^2} \frac{\partial^2 \dot{v}}{\partial x^2} \right) + \left( \frac{\partial^2 w}{\partial x^2} \frac{\partial^2 \dot{w}}{\partial x^2} \right) \right] dx \\
 & + \frac{1}{2} A_{11}^\psi \Omega \int_0^L \left[ \left( \frac{\partial^2 v}{\partial x^2} \frac{\partial^2 w}{\partial x^2} \right) - \left( \frac{\partial^2 w}{\partial x^2} \frac{\partial^2 v}{\partial x^2} \right) \right] dx
 \end{aligned} \tag{24}$$

where the second and the third terms are related to the hysteretic internal damping, and the terms  $A_{11}$  and  $A_{11}^\psi$  are given as follows:

$$\begin{cases} A_{11} = \frac{\pi}{4} \sum_{p=1}^P \bar{Q}_{11p} (R_p^4 - R_{p-1}^4) \\ A_{11}^\psi = \frac{\pi}{4} \sum_{p=1}^P \bar{Q}_{11p}^\psi (R_p^4 - R_{p-1}^4) \end{cases} \tag{25}$$

**4. Finite element formulation**

The developed shaft finite element has two nodes, as shown in Fig. 5. For each node, the element has four degrees of freedom: two displacements  $v$  and  $w$ , and two slopes  $\theta_y$  and  $\theta_z$  about  $y$  and  $z$  axes, respectively.

The nodal degrees of the freedom vector of the shaft element is given by (see Fig. 5):

$$\{q^e\} = \{v_1 \ w_1 \ \theta_{y1} \ \theta_{z1} \ v_2 \ w_2 \ \theta_{y2} \ \theta_{z2}\}^T \tag{26}$$

which, accordingly to the relations (17), includes the nodal vectors  $\{q_v^e\}$  and  $\{q_w^e\}$  given by:

$$\begin{aligned}
 \{q_v^e\} &= \{v_1 \ \theta_{z1} \ v_2 \ \theta_{z2}\}^T \\
 \{q_w^e\} &= \{w_1 \ -\theta_{y1} \ w_2 \ -\theta_{y2}\}^T
 \end{aligned} \tag{27}$$

The displacement functions  $v$  and  $w$  at the finite element domain are interpolated as:

$$v = [N] \{q_v^e\} \quad \text{and} \quad w = [N] \{q_w^e\} \tag{28}$$

where  $[N]$  is the shape function matrix. Under the Euler–Bernoulli beam hypothesis [22] and considering the transverse shear effect through the parameter  $\Phi$ , the shape function matrix is defined as:

$$[N] = \frac{1}{4(1 + \Phi)} [N_1 \quad N_2 \quad N_3 \quad N_4] \tag{29}$$

Using the normalized coordinate  $\xi \in [-1, 1]$  with its origin at  $x = L_e/2$ , the one-dimensional interpolation functions in terms of the normalized coordinate are defined as:

$$\begin{cases} N_1 = 2 - 3\xi + \xi^3 + 2\Phi(1 - \xi) \\ N_2 = J(1 - \xi - \xi^2 + \xi^3 + \Phi(1 - \xi^2)) \\ N_3 = 2 + 3\xi - \xi^3 + 2\Phi(1 + \xi) \\ N_4 = J(-1 - \xi + \xi^2 + \xi^3 - \Phi(1 - \xi^2)) \end{cases} \tag{30}$$

where  $J$  is the Jacobian of the transformation.

For a composite shaft, the transverse shear effect parameter  $\Phi$ , presented in Equations (29) and (30), is given by [23]:

$$\Phi = \frac{12A_{11}}{k_s(A_{55} + A_{66})L_e^2} \tag{31}$$

where the term  $A_{11}$  is defined in Equation (25) and the terms  $A_{55}$  and  $A_{66}$ , including the contribution of each orthotropic layer, are given as follows:

$$\begin{cases} A_{55} = \pi \sum_{p=1}^P \bar{Q}_{55p} (R_p^2 - R_{p-1}^2) \\ A_{66} = \pi \sum_{p=1}^P \bar{Q}_{66p} (R_p^2 - R_{p-1}^2) \end{cases} \tag{32}$$

#### 4.1. Elementary mass and gyroscopic matrices

The rotating shaft kinetic energy described in Equation (13) can be expressed as the sum of the elemental kinetic energy leading to the definition of the elementary mass and gyroscopic matrices. Adding the contribution of all the  $E$  finite elements, the kinetic energy can be expressed as:

$$T = \sum_{e=1}^E T^e \tag{33}$$

Using the interpolation (28) for the displacement functions  $v$  and  $w$  and the kinetic energy expression (13), the elemental kinetic energy  $T^e$  can be expressed as:

$$\begin{aligned} T^e &= \frac{1}{2} I_m \int_0^{L_e} \left[ \{\dot{q}_v^e\}^T [N]^T [N] \{\dot{q}_v^e\} + \{\dot{q}_w^e\}^T [N]^T [N] \{\dot{q}_w^e\} \right] dx \\ &+ \frac{1}{2} I_d \int_0^{L_e} \left[ \{\dot{q}_v^e\}^T \frac{d}{dx} [N]^T \frac{d}{dx} [N] \{\dot{q}_v^e\} + \{\dot{q}_w^e\}^T \frac{d}{dx} [N]^T \frac{d}{dx} [N] \{\dot{q}_w^e\} \right] dx \\ &- I_p \Omega \int_0^{L_e} \left[ \{q_v^e\}^T \frac{d}{dx} [N]^T \frac{d}{dx} [N] \{q_w^e\} \right] dx \end{aligned} \tag{34}$$

So, the kinetic energy can be written as:

$$T = \sum_{e=1}^E T^e = \sum_{e=1}^E \left( \frac{1}{2} \{\dot{q}^e\}^T [M^e] \{\dot{q}^e\} + \frac{1}{2} \{q^e\}^T [G^e(\Omega)] \{q^e\} \right) \tag{35}$$

where  $[M^e]$  is the elementary mass matrix and  $[G^e(\Omega)]$  is the elementary gyroscopic matrix, which are expressed in Appendix A (respectively, Equations (45) and (46)).

4.2. Elementary stiffness, dissipation and circulation matrices

The deformation energy described in Equation (24) can be expressed as the sum of the elemental deformation energy leading to the definition of the elementary stiffness, dissipation and circulation matrices. Adding the contribution of all the  $E$  finite elements, the deformation energy can be expressed as:

$$\Pi = \sum_{e=1}^E \Pi^e \tag{36}$$

Using the interpolation (28) for the displacement functions  $v$  and  $w$  and the deformation energy expression (24), the elemental internally damped composite shaft deformation energy  $\Pi^e$  can be expressed as:

$$\begin{aligned} \Pi^e = & \frac{1}{2} A_{11} \int_0^{L_e} \left[ \{q_v^e\}^T \frac{d^2}{dx^2} [N]^T \frac{d^2}{dx^2} [N] \{q_v^e\} + \{q_w^e\}^T \frac{d^2}{dx^2} [N]^T \frac{d^2}{dx^2} [N] \{q_w^e\} \right] dx \\ & + \frac{1}{2} A_{11}^\psi \int_0^{L_e} \left[ \{q_v^e\}^T \frac{d^2}{dx^2} [N]^T \frac{d^2}{dx^2} [N] \{\dot{q}_v^e\} + \{q_w^e\}^T \frac{d^2}{dx^2} [N]^T \frac{d^2}{dx^2} [N] \{\dot{q}_w^e\} \right] dx \\ & + \frac{1}{2} A_{11}^\psi \Omega \int_0^{L_e} \left[ \{q_v^e\}^T \frac{d^2}{dx^2} [N]^T \frac{d^2}{dx^2} [N] \{q_w^e\} - \{q_w^e\}^T \frac{d^2}{dx^2} [N]^T \frac{d^2}{dx^2} [N] \{q_v^e\} \right] dx \end{aligned} \tag{37}$$

So, the internally damped composite shaft deformation energy can be written as:

$$\Pi = \sum_{e=1}^E \Pi^e = \sum_{e=1}^E \left( \frac{1}{2} \{q^e\}^T [K^e] \{q^e\} + \frac{1}{2} \{q^e\}^T [H_d^e] \{\dot{q}^e\} + \frac{1}{2} \{q^e\}^T [H_c^e(\Omega)] \{q^e\} \right) \tag{38}$$

where  $[K^e]$  is the elementary stiffness matrix and  $[H_d^e]$  and  $[H_c^e(\Omega)]$  are the elementary matrices related to the hysteretic internal damping, which are expressed in Appendix B (respectively, Equations (49), (50) and (51)).

5. Equation of motion

The development for the definition of the equation of motion of the hysteretic damped rotating system is given in Appendix C; it is expressed as follows:

$$[M]\{\ddot{q}\} + ([G(\Omega)] + [K_d])\{\dot{q}\} + ([K] + [K_c(\Omega)])\{q\} = \{0\} \tag{39}$$

where spatial matrices are of order  $n$  for an  $n$ -degree-of-freedom system.

The dynamic equilibrium equation (39) can be written in the first-order form as:

$$[A]\{\dot{x}\} + [B(\Omega)]\{x\} = \{0\} \tag{40}$$

which is the state-space form of the equation of motion, where the  $2n \times 2n$  matrix  $[A]$  is a real symmetric positive definite matrix, the  $2n \times 2n$  matrix  $[B]$  is a real non-symmetric matrix, and the  $2n$  vector  $\{x\}$  is the state-space vector, defined as:

$$[A] = \begin{bmatrix} [M] & [0] \\ [0] & [M] \end{bmatrix}, \quad [B(\Omega)] = \begin{bmatrix} [0] & -[M] \\ [K] + [K_c(\Omega)] & [G(\Omega)] + [K_d] \end{bmatrix}, \quad \{x\} = \begin{Bmatrix} q \\ \dot{q} \end{Bmatrix} \tag{41}$$

The solutions to Equation (40) can be assumed to be:

$$\{x\} = \{X\} e^{\lambda t} \tag{42}$$

which, after introduction in (40), leads to the generalized eigenvalue problem:

$$[B(\Omega)]\{X\} = -\lambda[A]\{X\} \tag{43}$$

which has  $2n$  eigensolutions  $(\lambda_r, X_r)$ . The eigenvalues  $\lambda_r$  are obtained as  $n$  pairs of complex conjugates of the form:

$$\lambda_r = \mu_r \pm j\omega_r \tag{44}$$

where the imaginary parts  $\omega_r$  are the natural frequencies and the real parts  $\mu_r$  characterise the stability of the system. In fact, if  $\mu_r > 0$ , the system is unstable [11].

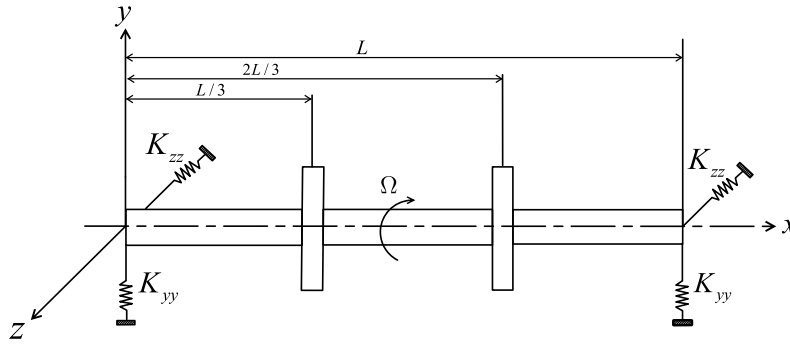


Fig. 6. Composite shaft with two discs supported by two bearings.

Table 1

Carbon/epoxy shaft material properties.

$E_1$ (GPa)	$E_2$ (GPa)	$G_{ij}$ (GPa)	$\nu_{12}$	$\rho$ (kg/m <sup>3</sup> )	$\psi_1$ (%)	$\psi_2$ (%)	$\psi_{12}$ (%)
172.7	7.2	3.76	0.3	1446.2	0.45	4.22	7.05

Table 2

Stacking sequence effects on the fundamental natural frequency (Hz) and the instability threshold (rpm).

Stacking sequence	$\omega_1$ (Hz)			Instability threshold (rpm)		
	EMBT [11]	SHBT [14]	ESLT	EMBT [11]	SHBT [14]	ESLT
1: [ $\pm 75$ ] <sub>8S</sub>	16.88	16.88	17.22	1167	1167	1210
2: [90 <sub>2</sub> , 45, 0] <sub>S</sub>	42.76	39.87	42.20	6956	5864	6481
3: [90, 0, 90, 45, 90, 45, 0, 90]	42.76	40.08	42.41	6965	5913	6559
4: [90, 45, 0 <sub>2</sub> ] <sub>S</sub>	52.37	50.71	51.79	12064	10981	11060
5: [0 <sub>2</sub> , 45 <sub>2</sub> , 90 <sub>2</sub> , 0 <sub>2</sub> ]	53.37	50.91	51.83	12064	11106	11084
6: [0 <sub>2</sub> , 90, 45] <sub>S</sub>	52.37	50.92	51.96	12064	11111	11165
7: [45, 0, 45, 0, 90, 0, 90, 0]	52.37	51.36	52.07	12064	11395	11235

## 6. Results and discussion

### 6.1. Validation case study – stacking sequence effects

The test rotor, studied first by Pereira and Silveira [11] and then by Sino et al. [14], which is a composite shaft with two rigid steel discs supported by two bearings at the ends as shown in Fig. 6, is considered.

This structure presents the following geometric and material properties:

- carbon/epoxy shaft:  $L = 1.2$  m, outer radius = 0.048 m, wall thickness = 0.008 m; shear correction factor:  $k_s = 1/2$ <sup>1</sup>;
- steel disk: inner radius = 0.048 m, outer radius = 0.15 m, thickness = 0.05 m;
- anisotropic bearings:  $K_{yy} = 1 \times 10^8$  N/m,  $K_{zz} = 1 \times 10^7$  N/m,  $K_{yz} = K_{zy} = 0$  N/m.

The carbon/epoxy shaft material properties are given in Table 1.

Table 2 gives the fundamental natural frequency and the instability threshold obtained from the proposed finite element based on ESLT for different stacking sequences in symmetric as well as non-symmetric configurations with eight layers of equal thickness, and presents a comparison between the results obtained using ESLT and those available in the literature using EMBT, as proposed by Pereira and Silveira [11] and SHBT proposed by Sino et al. [14].

The instability thresholds obtained using ESLT shown in Table 2 are determined from Fig. 7, where the real parts of the complex eigenvalues are presented as a function of the rotational speed of the rotor. In fact, when the real parts of the complex eigenvalues become positive, instability occurs.

It appears from Table 2 that the obtained results are in good agreement with those obtained using both theories and are closer to the ones obtained by Pereira and Silveira [11] using a formulation based on EMBT. In fact, Pereira and Silveira [11] used Euler–Bernoulli’s theory based on EMBT, excluding the transverse shear. Actually, Singh and Gupta [17,18] showed that EMBT is quite adequate for the estimation of the dynamic behaviour of rotating composite shafts, but predicts inaccurate results for non-symmetric stacking sequences. On the other hand, the SHBT proposed by Sino et al. [14] used Timoshenko’s

<sup>1</sup> For thin tubes:  $k_s = 1/2$  [8,19,24].

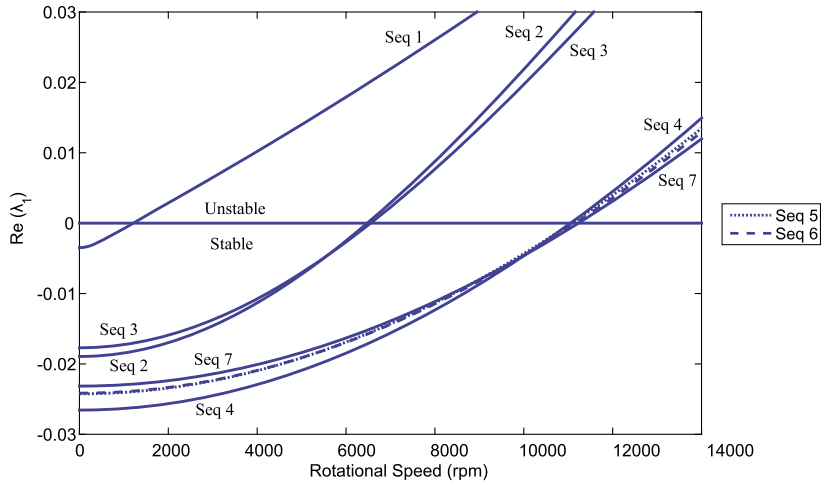


Fig. 7. Real part of the complex eigenvalue of the first forward mode.

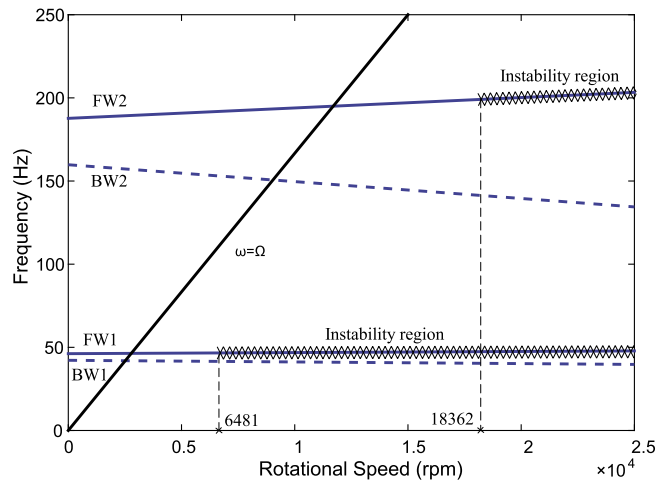


Fig. 8. Campbell diagram: second stacking sequence  $[90_2, 45, 0]_s$ .

beam theory, considering the transverse shear effects and the stacking sequence effects. However, the formulation developed in this work employs Euler–Bernoulli’s shaft theory based on ESLT, including transverse shear and the stacking sequence effects as well as hysteretic internal damping effects. It can be concluded that the developed Euler–Bernoulli finite element formulation based on ESLT is adequate for the dynamic and stability analysis of rotating composite shafts considering transverse shear, stacking sequence, and hysteretic internal damping effects.

Stacking sequences 2–3 are composed of four layers with fiber orientations at  $90^\circ$ , two layers at  $45^\circ$ , and two layers at  $0^\circ$ , whereas stacking sequences 4–7 are composed of four layers with fiber orientations at  $0^\circ$ , two layers at  $45^\circ$ , and two layers at  $90^\circ$ . Each layer contributes as a function of its fiber orientation and of its distance from the longitudinal shaft axis. When comparing stacking sequences 2 to 7, differences of 19% for the fundamental natural frequency and 42% for the associated instability threshold are obtained. When comparing the instability threshold values obtained for the stacking sequence 1 with 2 and those obtained for the stacking sequence 3 with 4, 5, 6 and 7 (see Table 2), it can be shown that the greater the number of layers with fibers oriented at  $90^\circ$  and positioned at the outer and the inner radius, the more the instability may appear at lower rotational speed.

A modal analysis is performed to see the effects of changing rotational speeds, from a non-rotating to a high rotational speed and to follow the frequencies associated with the bending modes. Figs. 8 and 9 show the Campbell diagrams for forward and backward natural frequencies over a wide speed range for the second and the fifth stacking sequences respectively (see Table 2). From this figures, it can be observed that the frequencies of the bending modes do change over the rotational speed range. The backward mode (BW) decreases in frequency, while the forward mode (FW) increases.

The Campbell diagrams, corresponding to the second and the fifth stacking sequence (see Table 2) that are shown respectively in Figs. 8 and 9, perform the evolution of natural frequencies with rotational speeds and explain the meaningful influence of stacking sequences on natural frequencies, critical speeds, and instability thresholds. Variations of 18% for

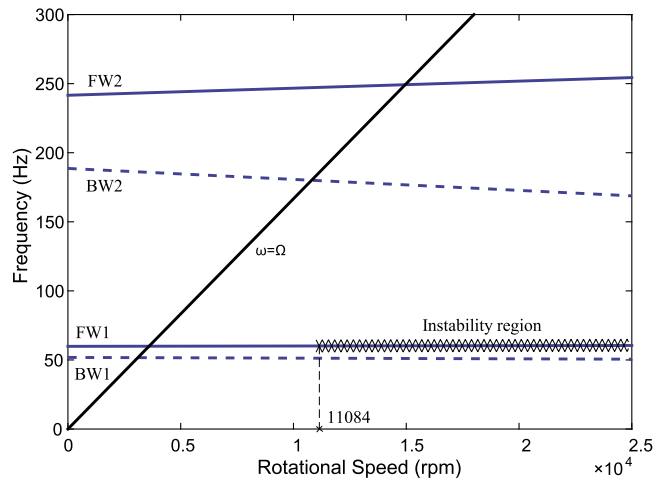


Fig. 9. Campbell diagram: fifth stacking sequence  $[0_2, 45_2, 90_2, 0_2]$ .

fundamental natural frequencies and 41% for the instability thresholds are obtained when comparing the second and the fifth stacking sequences. As it is expected, for different stacking sequences, the instability appears only in the supercritical ranges of the forward bending modes (FW). The backward bending modes (BW) are stable for all the rotational speeds. For the second stacking sequence, instability occurs in the first and the second forward bending modes (FW1 and FW2), whereas, for the fifth stacking sequence, instability occurs just in the first forward bending mode (FW1) in the considered rotational speed range. For the fifth stacking sequence, critical speeds are higher than those of the second stacking sequence, and the rotor speed surpasses the third critical speed, without producing rotor instability, while, for the second stacking sequence, instability appears following the second critical speed. This behaviour is explained by the fact that the greater the number of layers with fibers oriented at  $90^\circ$  and positioned at the outer and the inner radius such as the second stacking sequence  $[90_2, 45, 0]_S$ , the more instability may appear at lower rotational speed. Consequently, it can be concluded that the greater the number of layers with fibers oriented close to the longitudinal direction of the shaft (fibers oriented at  $0^\circ$ ) and positioned at the outer and the inner radius of the shaft, the more they contribute to the shaft rigidity and, therefore, the higher natural frequencies and critical speeds are, and the lower the internal composite materials damping is and, thus, the more instability appears at higher rotational speed.

### 6.2. Fiber orientation effects

In order to show the effects of fiber orientations on natural frequencies, critical speeds and instability threshold, a rotor with the same geometric and material properties as the test rotor (see Section 6.1) with two rigid steel discs and supported by two isotropic bearings at the ends ( $K_{yy} = K_{zz} = 1 \times 10^8$  N/m) is considered. The stacking sequence of the composite material consists of one layer  $[\alpha]$ . Fig. 10 shows the Campbell diagram of the first pairs of the bending mode and the rotor instability region (symbolized by a dashed line).

It can be observed from Fig. 10 that the backward modes (BW) are stable at all rotational speeds, whereas the forward modes (FW) destabilize from the first critical speed. Fig. 11 shows the instability threshold for different fiber orientations. The instability region corresponds to the region above the curve.

As it was concluded in the above sections, the higher is the fiber orientation angle, higher is the internal damping of the composite material matrix, and therefore instability occurs at lower rotational speed. It can be observed from both Figs. 10 and 11 that, for small fiber orientation angles, the internal composite material damping has a lesser influence on rotor instability, which occurs at higher rotational speed compared to the large fiber orientation angles. It can be concluded that the closer the fiber is oriented to the longitudinal direction of the shaft, the higher the natural frequencies and critical speeds are; at higher rotational speeds, rotor instability appears.

### 6.3. Effects of the properties of the bearings

To analyse the combined influence of internal composite material damping and of damping by external bearings on natural frequencies, critical speeds, and instability thresholds, a rotor with the same geometric and material properties as the test rotor (see Section 6.1) with two rigid steel discs and supported by two isotropic bearings at the ends is considered. As the bearings are isotropic, their stiffness and their damping are the same in two orthogonal directions:  $K_{yy} = K_{zz} = 1 \times 10^8$  N/m and  $C_{yy} = C_{zz}$ . Isotropic bearings with coupled terms  $K_{yz} = K_{zy} = 1 \times 10^7$  N/m are also considered. The composite shaft stacking sequence is balanced and symmetric, with eight layers of equal thickness:  $[\pm 15]_{8S}$ .

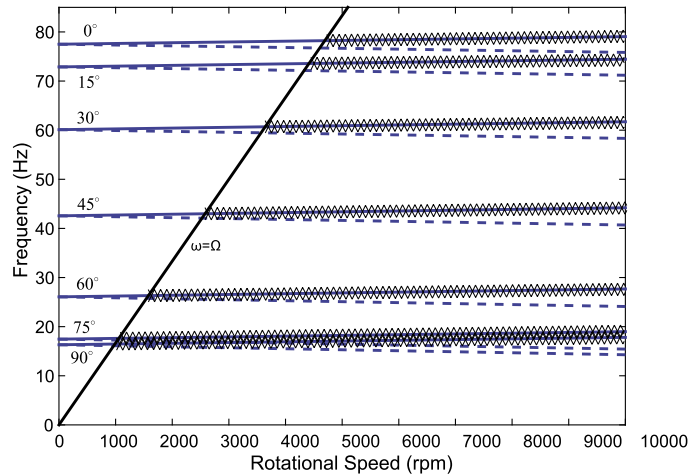


Fig. 10. Fiber orientation effects on the first bending mode of the rotating composite shaft (– FW1; - - BW1).

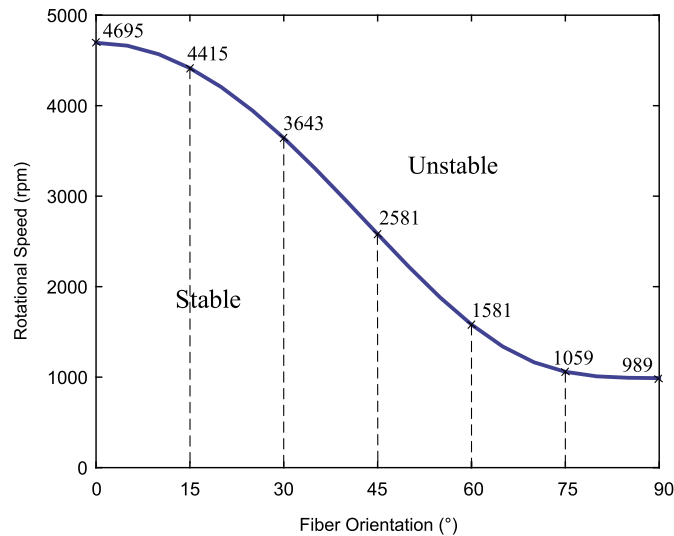


Fig. 11. Rotor instability region for different fiber orientations.

Considering isotropic bearings without external damping, Fig. 12 shows the Campbell diagram of the rotating composite shaft supported by isotropic bearings, while Fig. 13 shows the Campbell diagram of the rotating composite shaft supported by isotropic bearings with coupled terms.

It can be seen from Fig. 12 that instability occurs at the critical speeds for the forward modes (FW), while, comparing Figs. 12 and 13, it can be observed that the associated coupling terms destabilize the forward modes at rotational speeds slightly higher than the critical speeds.

Considering now isotropic bearings with external damping, Figs. 14 and 15 show the Campbell diagrams of the rotating composite shaft supported by isotropic bearings with different values of external damping. It can be observed that the external damping introduced by the bearings increases quite the threshold instability and that, for higher external damping, the rotor would be stable at all rotational speeds, as shown in Fig. 15.

Fig. 16 shows the Campbell diagrams of the rotating composite shaft supported by isotropic bearings with external damping and coupled terms. Comparing Figs. 14 and 16, it can be observed that the coupled terms introduced by the bearings increase slightly the threshold instability. It can be concluded that rotor stability is improved by increasing the damping and the coupled terms provided by the bearings, whereas increasing internal composite material damping may reduce the instability threshold.

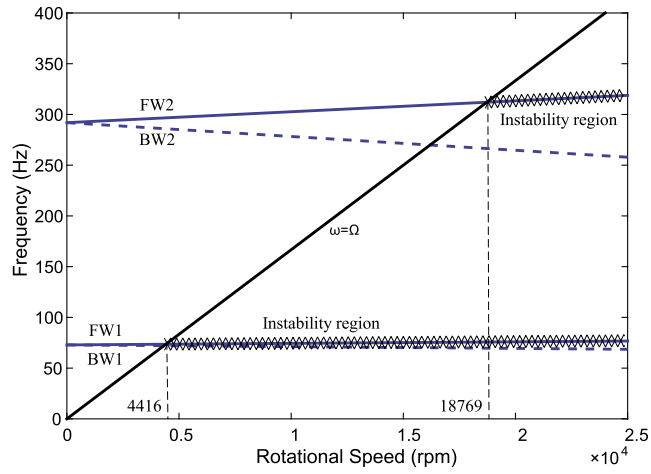


Fig. 12. Case: isotropic bearings without external damping and coupled terms.

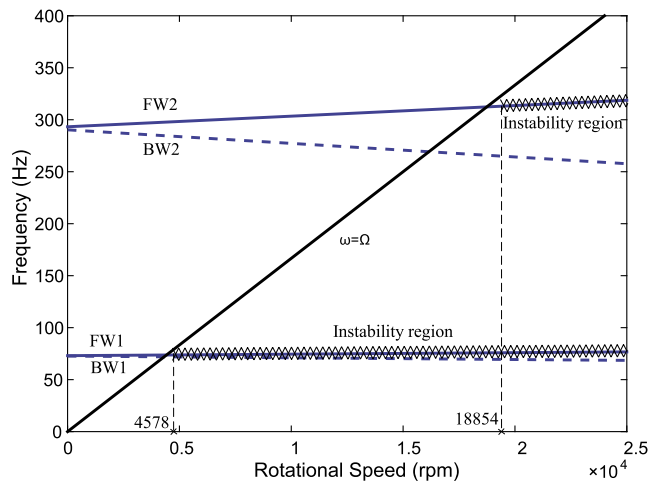


Fig. 13. Case: isotropic bearings without external damping and with coupled terms  $K_{yz} = K_{zy} = 1 \times 10^7$  N/m.

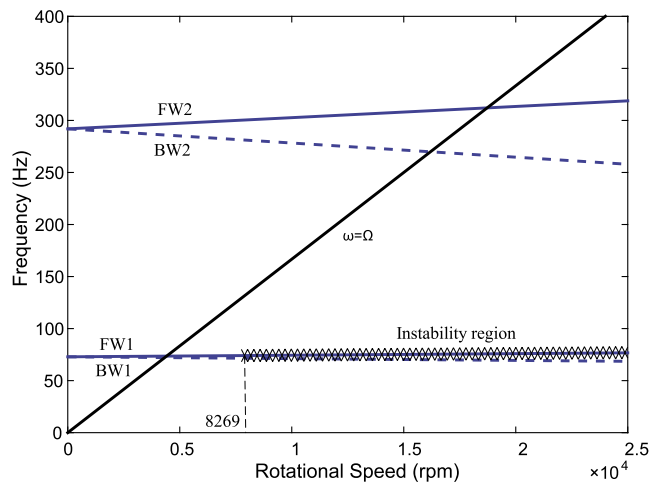


Fig. 14. Case: isotropic bearings without coupled terms and with external damping  $C_{yy} = C_{zz} = 1 \times 10^2$  N/m/s.

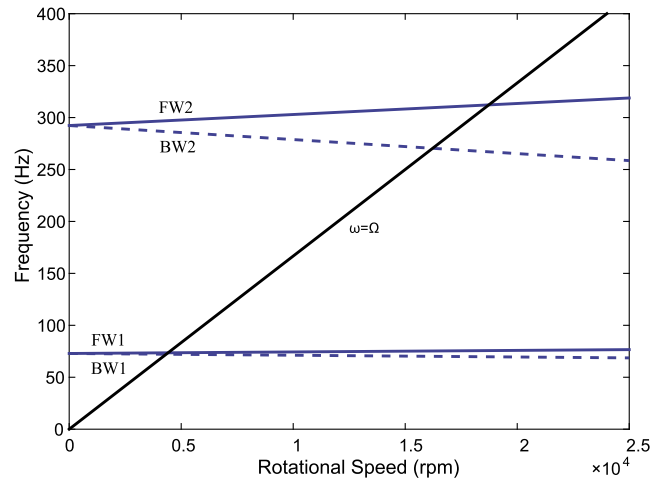


Fig. 15. Case: isotopic bearings without coupled terms and with external damping  $C_{yy} = C_{zz} = 1 \times 10^4$  N/m/s.

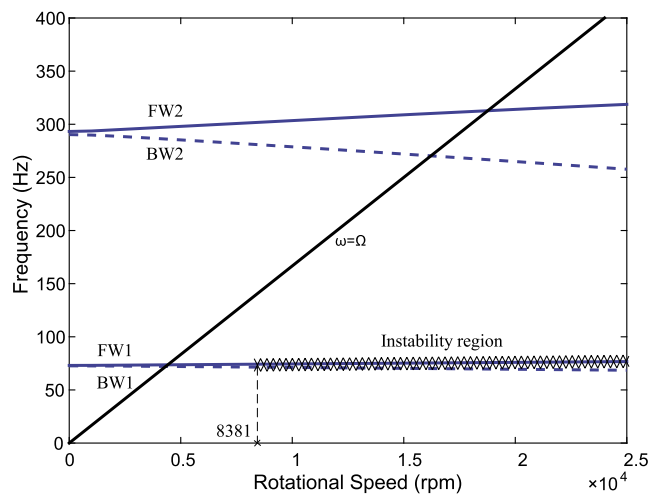


Fig. 16. Case: isotopic bearings with external damping  $C_{yy} = C_{zz} = 1 \times 10^2$  N/m/s and coupled terms  $K_{yz} = K_{zy} = 1 \times 10^7$  N/m.

## 7. Conclusion

This work deals with the stability analysis of internally damped rotating composite shafts. Euler–Bernoulli's shaft finite element formulation based on Equivalent Single Layer Theory (ESLT) is developed and compared to Equivalent Modulus Beam Theory (EMBT) and Simplified Homogenized Beam Theory (SHBT). The agreement has been found to be good in terms of natural frequencies and instability threshold compared with results available in the literature using different theories. The developed formulation considers the effects of fiber orientation, stacking sequence for symmetric as well as non-symmetric configurations, transverse shear and hysteretic internal damping of the composite material. A study of the effects of different parameters on the natural frequencies, critical speeds, and instability threshold of rotating composite shafts is carried out. This analysis illustrates that the higher is the fiber orientation angle, the higher is the internal damping introduced by the composite material, and therefore, the instability regions appear at lower rotational speed. This study highlights also that rotor stability can be improved by increasing bearing damping, although increasing internal material damping can reduce the instability threshold. Consequently, fiber orientation, stacking sequence and bearing properties are considered as optimization parameters for the dynamic behaviour and, in particular, for the stability analysis of internally damped rotating composite shafts.

## Acknowledgements

This work has been funded by the Tunisia/Portugal research cooperation program. The authors gratefully acknowledge the funding by Project NORTE-01-0145-FEDER-000022 – SciTech – Science and Technology for Competitive and Sustain-

able Industries, cofinanced by the “Programa Operacional Regional do Norte” (NORTE2020) through the “Fundo Europeu de Desenvolvimento Regional” (FEDER).

#### Appendix A. Elementary mass matrix $[M^e]$ and elementary gyroscopic matrix $[G^e(\Omega)]$

$$[M^e] = \frac{L_e}{840(1+\Phi)^2} \begin{bmatrix} M_1 & 0 & 0 & M_2 & M_3 & 0 & 0 & M_4 \\ & M_1 & -M_2 & 0 & 0 & M_3 & -M_4 & 0 \\ & & M_5 & 0 & 0 & M_4 & M_6 & 0 \\ & & & M_5 & -M_4 & 0 & 0 & M_6 \\ & & & & M_1 & 0 & 0 & -M_2 \\ & \text{Sym.} & & & & M_1 & M_2 & 0 \\ & & & & & & M_5 & 0 \\ & & & & & & & M_5 \end{bmatrix} \quad (45)$$

$$[G^e(\Omega)] = \frac{I_p \Omega}{60L_e(1+\Phi)^2} \begin{bmatrix} 0 & G_1 & G_2 & 0 & 0 & -G_1 & G_2 & 0 \\ & 0 & 0 & G_2 & G_1 & 0 & 0 & G_2 \\ & & 0 & G_3 & G_2 & 0 & 0 & G_4 \\ & & & 0 & 0 & G_2 & -G_4 & 0 \\ & & & & 0 & G_1 & -G_2 & 0 \\ & \text{Skew-Sym.} & & & & 0 & 0 & -G_2 \\ & & & & & & 0 & G_3 \\ & & & & & & & 0 \end{bmatrix} \quad (46)$$

The elementary mass components presented in Equation (45) are given by:

$$\begin{cases} M_1 = I_m (312 + 588\Phi + 280\Phi^2) + \frac{1008 I_d}{L_e^2} \\ M_2 = -I_m L_e (44 + 77\Phi + 35\Phi^2) - \frac{(84 - 420\Phi) I_d}{L_e} \\ M_3 = I_m (108 + 252\Phi + 140\Phi^2) - \frac{1008 I_d}{L_e^2} \\ M_4 = I_m L_e (26 + 63\Phi + 35\Phi^2) - \frac{(84 - 420\Phi) I_d}{L_e} \\ M_5 = I_m L_e^2 (8 + 14\Phi + 7\Phi^2) + I_d (112 + 140\Phi + 280\Phi^2) \\ M_6 = -I_m L_e^2 (6 + 14\Phi + 7\Phi^2) - I_d (28 + 140\Phi - 140\Phi^2) \end{cases} \quad (47)$$

and the elementary gyroscopic terms presented in Equation (46) are given by:

$$\begin{cases} G_1 = -72 \\ G_2 = -L_e (6 - 30\Phi) \\ G_3 = -L_e^2 (8 + 10\Phi + 20\Phi^2) \\ G_4 = L_e^2 (2 + 10\Phi - 10\Phi^2) \end{cases} \quad (48)$$

#### Appendix B. Elementary stiffness matrix $[K^e]$ and elementary matrices related to the hysteretic internal damping $[H_d^e]$ and $[H_c^e(\Omega)]$

$$[K^e] = \frac{A_{11}}{(1+\Phi)L_e^3} \begin{bmatrix} 12 & 0 & 0 & -6L_e & -12 & 0 & 0 & -6L_e \\ & 12 & 6L_e & 0 & 0 & -12 & 6L_e & 0 \\ & & (4+\Phi)L_e^2 & 0 & 0 & -6L_e & (2-\Phi)L_e^2 & 0 \\ & & & (4+\Phi)L_e^2 & 6L_e & 0 & 0 & (2-\Phi)L_e^2 \\ & \text{Sym.} & & & 12 & 0 & 0 & 6L_e \\ & & & & & 12 & -6L_e & 0 \\ & & & & & & (4+\Phi)L_e^2 & 0 \\ & & & & & & & (4+\Phi)L_e^2 \end{bmatrix} \quad (49)$$

$$\begin{aligned}
 [H_d^e] &= \frac{A_{11}^\psi}{(1 + \Phi)L_e^3} \begin{bmatrix} 12 & 0 & 0 & -6L_e & -12 & 0 & 0 & -6L_e \\ 12 & 6L_e & & 0 & 0 & -12 & 6L_e & 0 \\ & (4 + \Phi)L_e^2 & & 0 & 0 & -6L_e & (2 - \Phi)L_e^2 & 0 \\ & & (4 + \Phi)L_e^2 & 6L_e & 0 & 0 & 0 & (2 - \Phi)L_e^2 \\ \text{Sym.} & & & 12 & 0 & 0 & 0 & 6L_e \\ & & & & 12 & -6L_e & 0 & 0 \\ & & & & & (4 + \Phi)L_e^2 & 0 & (4 + \Phi)L_e^2 \end{bmatrix} \quad (50) \\
 [H_c^e(\Omega)] &= \frac{A_{11}^\psi \Omega}{(1 + \Phi)L_e^3} \begin{bmatrix} 0 & -12 & -6L_e & 0 & 0 & 12 & -6L_e & 0 \\ & 0 & 0 & -6L_e & -12 & 0 & 0 & -6L_e \\ & & 0 & -(4 + \Phi)L_e^2 & -6L_e & 0 & 0 & -(2 - \Phi)L_e^2 \\ & & & 0 & 0 & -6L_e & (2 - \Phi)L_e^2 & 0 \\ \text{Skew-Sym.} & & & & 0 & -12 & 6L_e & 0 \\ & & & & & 0 & 0 & 6L_e \\ & & & & & & 0 & -(4 + \Phi)L_e^2 \\ & & & & & & & 0 \end{bmatrix} \quad (51)
 \end{aligned}$$

**Appendix C. Equation of motion**

The relation between the elemental degrees of freedom  $\{q^e\}$  and the global degrees of freedom  $\{q\}$  is established through the connectivity matrices  $[R^e]$ , expressed as follows:

$$\{q^e\} = [R^e] \{q\} \quad (52)$$

Introducing the connectivity (52) into the expression of kinetic energy (35) gives:

$$T = \frac{1}{2} \{\dot{q}\}^T [M] \{\dot{q}\} + \frac{1}{2} \{q\}^T [G(\Omega)] \{q\} \quad (53)$$

where the assembled global mass  $[M]$  and gyroscopic  $[G(\Omega)]$  matrices are defined by:

$$\begin{cases} [M] = \sum_{e=1}^E [R^e]^T [M^e] [R^e] \\ [G(\Omega)] = \sum_{e=1}^E [R^e]^T [G^e(\Omega)] [R^e] \end{cases} \quad (54)$$

Introducing also the connectivity (52) into the expression of internally damped composite shaft deformation energy (38) gives:

$$\Pi = \frac{1}{2} \{q\}^T [K] \{q\} + \frac{1}{2} \{\dot{q}\}^T [H_d] \{\dot{q}\} + \frac{1}{2} \{q\}^T [H_c(\Omega)] \{q\} \quad (55)$$

where the assembled stiffness matrix  $[K]$  and the assembled matrices related to the hysteretic internal damping matrices  $[H_d]$  and  $[H_c(\Omega)]$  are defined by:

$$\begin{cases} [K] = \sum_{e=1}^E [R^e]^T [K^e] [R^e] \\ [H_d] = \sum_{e=1}^E [R^e]^T [H_d^e] [R^e] \\ [H_c(\Omega)] = \sum_{e=1}^E [R^e]^T [H_c^e(\Omega)] [R^e] \end{cases} \quad (56)$$

Applying Lagrange's equations to the expressions of kinetic energy (53) and of deformation energy (55) yields the following equation of motion for the hysteretic damped rotating system:

$$[M] \{\ddot{q}\} + ([G(\Omega)] + [H_d]) \{\dot{q}\} + ([K] + [H_c(\Omega)]) \{q\} = \{0\} \quad (57)$$

where  $[M]$  is the symmetric mass matrix,  $[G(\Omega)]$  is the skew-symmetric gyroscopic matrix, which is rotational speed  $\Omega$  dependent,  $[K]$  is the stiffness matrix, and  $[H_d]$  and  $[H_c(\Omega)]$  are the matrices related to hysteretic internal damping.  $\{\ddot{q}\}$ ,  $\{\dot{q}\}$  and  $\{q\}$  are respectively the nodal acceleration, nodal velocity and nodal displacement vectors.

Using the equivalence between hysteretic damping and viscous damping, the symmetric dissipation matrix  $[K_d]$  and the skew-symmetric circulation matrix  $[K_c(\Omega)]$ , which is rotational speed  $\Omega$  dependent, are obtained as follows [25]:

$$\begin{cases} [K_d] = \frac{1}{\pi} [H_d][\omega]^{-1} \\ [K_c(\Omega)] = \frac{1}{\pi} [H_c(\Omega)][\omega]^{-1} \end{cases} \quad (58)$$

where  $[\omega]$  is the diagonal natural frequencies matrix of the undamped non-rotating system [26].

Therefore, the equation of motion of the hysteretic damped rotating system can be written as follows:

$$[M]\{\ddot{q}\} + ([G(\Omega)] + [K_d])\{\dot{q}\} + ([K] + [K_c(\Omega)])\{q\} = \{0\} \quad (59)$$

## References

- [1] H. Wettergren, K. Olsson, Dynamic instability of a rotating asymmetric shaft with internal viscous damping supported in anisotropic bearings, *J. Sound Vib.* 195 (1996) 75–84.
- [2] O. Montagnier, C. Hochard, Dynamic instability of supercritical driveshafts mounted on dissipative supports-effects of viscous and hysteretic internal damping, *J. Sound Vib.* 305 (2007) 378–400.
- [3] H. Zinberg, M. Symonds, The development of an advanced composite tail rotor driveshaft, Presented at the 26th Annual Forum of the American Helicopter Society, Washington, DC, June 1970.
- [4] D. Lee, H. Kim, J. Kim, J. Kim, Design and manufacture of an automotive hybrid aluminum/composite drive shaft, *Compos. Struct.* 63 (2004) 87–99.
- [5] R. Moorthy, Y. Mitiku, K. Sridhar, Design of automobile driveshaft using carbon/epoxy and kevlar/epoxy composites, *Amer. J. Eng. Res.* 2 (2013) 173–179.
- [6] V. Bhajantri, S. Bajantri, A. Shindolkar, S. Amarapure, Design and analysis of composite drive shaft, *Int. J. Res. Eng. Technol.* 3 (2014) 738–745.
- [7] J. Gindele, W. Novak, P. Fietkau, P. Neuwirth, W. Leitermann, The transaxle powertrain of the mercedes-amg sports cars, 2015.
- [8] H. Gubran, K. Gupta, The effect of stacking sequence and coupling mechanisms on the natural frequencies of composite shafts, *J. Sound Vib.* 282 (2005) 231–248.
- [9] V. Alwan, A. Gupta, A. Sekhar, R. Velmurugan, Dynamic analysis of shafts of composite materials, *J. Reinf. Plast. Compos.* 29 (2010) 3364–3379.
- [10] B.L. Newkirk, Shaft whipping, *Gen. Electr. Rev.* 27 (1924) 169–178.
- [11] J. Pereira, M. Silveira, Evaluation and optimization of the instability regions on rotors in wounding shaft, in: II National Congress of Mechanical Engineering, 2002, pp. 315–320.
- [12] G. Genta, On a persistent misunderstanding of the role of hysteretic damping in rotordynamics, *J. Vib. Acoust.* 126 (2004) 459–461.
- [13] F. Vatta, A. Vigliani, Internal damping in rotating shafts, *Mech. Mach. Theory* 43 (2008) 1376–1384.
- [14] R. Sino, T. Baranger, E. Chatelet, G. Jacquet, Dynamic analysis of a rotating composite shaft, *Compos. Sci. Technol.* 68 (2008) 337–345.
- [15] G. Jacquet-Richardet, E. Chatelet, T. Nouri-Baranger, Rotating internal damping in the case of composite shafts, in: IUTAM Symposium on Emerging Trends in Rotor Dynamics, Springer, 2011, pp. 125–134.
- [16] J. Pereira, M. Silveira, Instability regions due to internal damping on rotors in wounding shaft, in: 21st Iberian Latin American Congress on Computational Methods in Engineering, 2000.
- [17] S. Singh, K. Gupta, Dynamic analysis of composite rotors, *Int. J. Rotating Mach.* 2 (1996) 179–186.
- [18] S. Singh, K. Gupta, Composite shaft rotordynamic analysis using a layerwise theory, *J. Sound Vib.* 191 (1996) 739–756.
- [19] S.B. Arab, J.D. Rodrigues, S. Bouaziz, M. Haddar, A finite element based on equivalent single layer theory for rotating composite shafts dynamic analysis, *Compos. Struct.* 178 (2017) 135–144.
- [20] J. Reddy, An evaluation of equivalent-single-layer and layerwise theories of composite laminates, *Compos. Struct.* 25 (1993) 21–35.
- [21] J. Reddy, *Mechanics of Laminated Composite Plates – Theory and Analysis*, CRC Press, 1997.
- [22] E. Hinton, D. Owen, *An Introduction to Finite Element Computation*, Pineridge Press Limited, 1981.
- [23] M.A. Musmani, *Rotordynamic Analysis of Tapered Composite Driveshaft Using Conventional and Hierarchical Finite Element Formulations*, Ph.D. thesis, Concordia University Montreal, Quebec, Canada, 2013.
- [24] J. Freund, A. Karakoc, Shear and torsion correction factors of timoshenko beam model for generic cross sections, *Res. Eng. Struct. Mater.* 2 (2016) 19–27.
- [25] M. Lalanne, P. Berthier, J.D. Hagopian, *Mécanique des vibrations linéaires*, Masson, 1986.
- [26] M.E. Silveira, *Análise do Comportamento Dinâmico de Rotores em Eixos Bobinados*, Master's thesis, Universidade Federal de Santa Catarina, Florianópolis, Brazil, 2001.